ADVANCED MATERIALS
www.advmat.de

Microfluidic Platform for Generating and Releasing Patient-Derived Cancer Organoids with Diverse Shapes: Insight into Shape-Dependent Tumor Growth

Sina Kheiri, Ilya Yakavets, Jennifer Cruickshank, Fatemeh Ahmadi, Hal K Berman, David W. Cescon, Edmond W.K. Young, and Eugenia Kumacheva**

Multicellular spheroids and patient-derived organoids find many applications in fundamental research, drug discovery, and regenerative medicine. Advances in the understanding and recapitulation of organ functionality and disease development require the generation of complex organoid models, including organoids with diverse morphologies. Microfluidics-based cell culture platforms enable time-efficient confined organoid generation. However, the ability to form organoids with different shapes with a subsequent transfer from microfluidic devices to unconstrained environments for studies of morphology-dependent organoid growth is yet to be demonstrated. Here, a microfluidic platform is introduced that enables high-fidelity formation and addressable release of breast cancer organoids with diverse shapes. Using this platform, the impact of organoid morphology on their growth in unconstrained biomimetic hydrogel is explored. It is shown that proliferative cancer cells tend to localize in high positive curvature organoid regions, causing their faster growth, while the overall growth pattern of organoids with diverse shapes tends to reduce interfacial tension at the organoid-hydrogel interface. In addition to the formation of organoids with diverse morphologies, this platform can be integrated into multi-tissue micro-physiological systems.

1. Introduction

Organoids are 3D cell cultures that recapitulate many aspects of the structure, function, and cellular complexity of human organs and tissues.[1] Over the past two decades, significant progress has been achieved in the initiation and growth of organoids from human adult stem cells and patient-derived tumor samples.[2–4] Organoids largely reproduced patient-specific intratumor heterogeneity, gene and protein expression, molecular signatures, metabolic activity, and tissue-like microstructures.[5,6] However, to better recapitulate organ functionality for fundamental and translational research, organoids with greater complexity are needed. Such complexity may include the incorporation of stromal and vasculature components, the ability to model stimulus-mediated changes in microenvironment over the organoid culture period, and the generation of organoids with

S. Kheiri, E. W. Young
Department of Mechanical & Industrial Engineering
University of Toronto
5 King's College Road, Toronto, ON M5S 3G8, Canada
E-mail: eyoung@mie.utoronto.ca

I. Yakavets, F. Ahmadi, E. Kumacheva
Department of Chemistry
University of Toronto
80 St. George Street, Toronto, ON M5S 3H6, Canada
E-mail: eugenia.kumacheva@utoronto.ca

The ORCID identification number(s) for the author(s) of this article can be found under https://doi.org/10.1002/adma.202410547

DOI: 10.1002/adma.202410547

J. Cruickshank, H. K Berman, D. W. Cescon
Princess Margaret Cancer Centre
University Health Network
610 University Avenue, Toronto, ON M5G 2C1, Canada

H. K Berman
Department of Laboratory Medicine and Pathobiology
University of Toronto
1 King's College Circle, Toronto, ON M5S 1A8, Canada

D. W. Cescon
Department of Medicine
University of Toronto
1 King's College Circle, Toronto, ON M5S 1A8, Canada

E. W. Young, E. Kumacheva
Institute of Biomedical Engineering
University of Toronto
164 College Street, Toronto, ON M5S 3G9, Canada

E. Kumacheva
Department of Chemical Engineering and Applied Chemistry
University of Toronto
200 College Street, Toronto, ON M5S 3E5, Canada

different sizes and shapes.[7,8] In particular, the importance of organoid shape has been established for intestinal organoids, whereby engineering cells to grow a tubular shape contributed to the longevity of organoid culture, as well emergence of specialized, rare microfold cells and spatial arrangement akin to the crypt-and villus-like domains that are observed in vivo.[9] Furthermore, the growth of intestinal organoids yielded crypt microstructures that were similar to those observed in vivo, where the location and number of crypts could be altered by varying the shape of multicellular aggregates of stem cells.[10]

Surface patterning techniques have been extensively used to explore the role of shapes on the growth and morphology of 2D multicellular aggregates.[11,12] The shape of human stem cell aggregates seeded on a patterned substrate was found to dictate the ultimate morphology of neural tube-like structures grown on this surface.[13] A narrow (less than 150 μm in width) rectangular pattern resulted in a U-shaped neural folding, while a wider rectangular pattern led to lateral hinges. A study of the growth of 2D multicellular patterns of prostate cancer cells on patterned surfaces revealed a higher expression of tumorigenic transcription factors (e.g., Oct4 and NanoG) in areas with a positive curvature at the edge of the pattern.[14] Integrin-mediated adhesion and mechanotransduction receptors activated a cancer stem cell-like phenotype in these regions. Recently, it has been shown that geometric cues at length scales of hundreds of micrometers can significantly affect cell migration, growth kinetics, and cancer invasion.[15,16] These results merit the development of strategies for the initiation and growth of 3D cancer spheroids and organoids with various shapes, which can be used to advance our understanding of cancer invasion.[17]

Cancer invasion represents a major hallmark of cancer progression.[18] Invasion occurs via different tumor cell migration modes. When cell-cell junctions weaken, individual cancer cells can dissociate from the tumor into the surrounding tissue by amoeboid or mesenchymal movement.[19] Alternatively, when cell-cell junctions are retained, tumor invasion can occur via collective cell movement.[20] This latter mode dominates in breast and lung cancer and is driven by protrusion forces at the leading edges of the tumor, stemming from actomyosin-mediated contractility of the invading front-line cells (known as "leader cells").[21,22] Studies of individual cell invasion have provided insight into single cell-driven cancer invasion,[23,24] however, the underlying processes of collective cancer invasion are not well understood.[25]

Cancer spheroids and organoids are generally grown in conventional tissue culture, bioreactors, spinning flasks, hanging drops, and microfluidic platforms;[26–29] however, the ability to form spheroids and organoids with non-spherical morphologies remains a challenge (here we refer to such spheroids as "tumoroids"[30] to distinguish them from classic spherical shape "spheroids"). Recently, a hanging drop method was used to generate non-spherical tumoroids by seeding the cells in annular triangular, square-, or circular-shaped wells with a central supporting micropost.[31] Due to cell compaction around this micropost, after 24-h culture, the tumoroids transformed into multiple fragments. Furthermore, this method did not provide a continuous fluidic supply of nutrients and oxygen and waste product removal required for long-term tumoroid culture.[32,33] Microfluidic platforms address the latter limitation, while also enabling the generation of uniformly sized tumoroids.[34–36] Currently, however, the formation of tumoroids with different shapes and their subsequent release from the microfluidic device for downstream bioanalyses such as flow cytometry, RNA sequencing, or histological staining have not yet been reported. The ability to achieve control over tumoroid shape and its targeted release from its culture environment would be highly desirable, allowing for advanced studies of cancer cell biology in a 3D morphologically-relevant context.[37]

Here we report a multi-layer microfluidic platform referred to as "**ReSCUE**" (**R**ecoverable-**S**pheroid-on-a-**C**hip with **U**nrestricted **E**xternal **S**hape) that enables the generation of uniformly sized tumoroids and organoids with different shapes and their selective release from the microfluidic device for studies of cancer cell invasion in unconstrained environments. Unlike previously reported microfluidic platforms for cancer spheroid and organoid formation, the ReSCUE platform enables their recovery in a targeted (addressable) manner, thus enabling the analysis of tumoroids and organoids of interest. Importantly, we show the application of ReSCUE for the generation, selective release, and downstream analysis of breast cancer patient-derived organoids (PDOs). For both tumoroids and PDOs, we show the utility of the ReSCUE platform for studies of the impact of tumor morphology on collective invasion.

2. Results

2.1. ReSCUE Microfluidic Platform

Building upon the "SlipChip" hydrodynamic droplet trapping approach,[38] we developed a microfluidic platform by using two hydrophobically modified thermoplastic layers stacked together but allowing for lateral slipping (sliding) with respect to each other (Figures S1 and S2, Supporting Information). The microwell layer (**Figure 1**A, bottom layer, pink color) contained microwells with different shapes. These microwells were used as templates for confining the loaded cells to generate multicellular tumoroids or PDOs with a desired shape. The channel layer (Figure 1A, top layer marked with blue color) contained complementary microfluidic ducts and a microchannel for cell culture. Prior to assembly, both layers were coated with silicone oil, a sealing agent preventing fluid leakage and a lubricant facilitating smooth sliding of the layers with respect to each other. The microwell and channel layers were assembled to superimpose the microwells and the complementary microfluidic ducts, thus creating a continuous fluidic path through the device (Figure S3, Supporting Information).

First, a suspension of MCF-7 cells, MCF-10A cells, or patient-derived cell lines (patient -line DCXBTO.58: ER-/PR-/HER2- and patient line BPTO.95: ER+/PR+/HER2-) was prepared in the mixture of the hydrogel precursors. Subsequently, this suspension was introduced in ReSCUE containing 6 loading channels, each accommodating 6 tumoroids or PDOs (Figure 1A, step 1). The microwell layer was shifted laterally with respect to the Channel layer to generate cell-laden droplets conforming to the shape of the microwells in the Microwell layer (Figure 1A, step 2). Following ReSCUE incubation for 2 h at 37 °C to allow for gel formation in the droplets, the cell culture media was continuously perfused through the device using gravity-driven flow

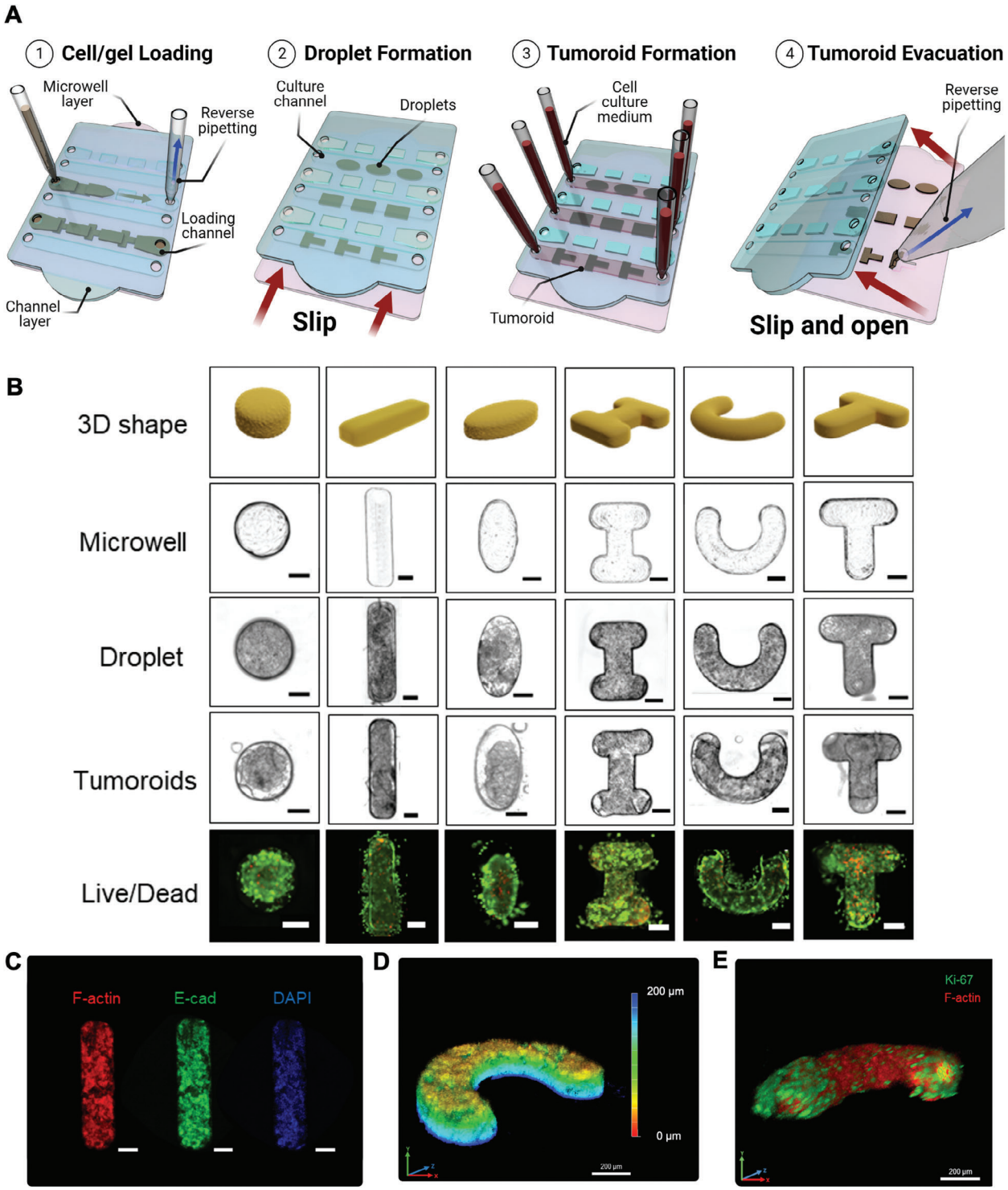

Figure 1. Generation of tumoroids using ReSCUE platform. A) Schematic of the ReSCUE platform: (1) assembly of the two-layer ReSCUE platform by superimposing the microwells in the lower microwell (pink) layer and complementary microducts in the upper channel layer (blue). The layers were coated with silicone oil seal to prevent fluid leakage. (2) Sliding of the channel layer to form cell-laden droplets acquiring the shape of the microwells, (3) perfusion of the cell culture medium through the device after 2-h incubation of the cell-laden droplets at 37 °C, and (4) lateral sliding of the channel layer to expose tumoroids for their release. B) Brightfield and fluorescence images of MCF-7 tumoroids with different shapes. The images were taken after 48 h of cell culture and stained with calcein-AM (green, live cells) and propidium iodide (red, dead cells). C) Immunostaining of rod-shaped MCF-7 tumoroids formed after 48-h cell culture with F-actin (red), E-cadherin (green), and DAPI (blue). D) Confocal microscopy images of U-shaped tumoroids formed and imaged in ReSCUE. Color bar represents the distance from the top surface of tumoroid. E) Confocal microscopy images of U-shaped tumoroids formed after 48-hr cell culture stained with F-actin (red) and Ki-67 (green) after their release. All scale bars are 200 µm.

(Figure 1A, step 3). After 2–4 days (depending on the cell type), the cell-laden microgels transformed into tumoroids or PDOs with a shape pre-determined by the microwell geometry. To release tumoroids from the wells, the Microwell layer was shifted laterally to expose the tumoroids or PDOs to the air and release them "on demand;" (Figure 1, step 4) by gentle pipetting with the cell culture medium under a brightfield microscope. We also explored the ability to form differently shaped stroma-rich co-cultures of MCF-7 and human dermal fibroblasts (Figure S10, Supporting Information).

To realize the ReSCUE platform, we focused first on tumoroids comprised of MCF-7 breast cancer cells. We fabricated disk-, rod-, oval-, U-, and I-shaped ducts in the microwell layer (Figure 1B, rows 1 and 2). The two layers of the ReSCUE were sealed, and cell-laden droplets were generated in the microwells by loading a suspension of cells in an aqueous mixture comprised of aldehyde-functionalized cellulose nanocrystals (a-CNCs) and gelatin (hydrogel precursors) and subsequently laterally slipping the layers of the microfluidic device (Figure 1B, row 3). Later in the text, this hydrogel is termed as "EKGel". The cell-laden microgels replicated the shape of the microwells with high fidelity and high cell viability after 48-h culture under gravity-driven flow [39] (Figure 1B, rows 4 and 5), yielding disk-, rod-, oval-, U-, and I-shaped tumoroids (*see* tumoroids with other shapes in Figure S4, Supporting Information). The formation of cell-cell junctions and the distribution of actin in the cytoskeleton of cells within the tumoroids were confirmed by immunofluorescence staining against E-cadherin and F-actin, respectively (Figure 1C). To verify tumoroid morphology, we cultured, recovered, and stained U-shaped tumoroids on F-actin and Ki-67, and used high-resolution confocal microscopy to visualize cytoskeleton filaments and proliferative tumorigenic cells, respectively (Figure 1D,E). The tumoroids had the desired 3D shape with a thickness of ≈200 µm, both in the microfluidic device and upon their release, close to the depth of the host microwells. The 3D reconstruction, along with the other imaging results, provided evidence that the loaded cells were distributed evenly within the tumoroids and filled the wells sufficiently to generate all the desired shapes with high fidelity.

2.2. Tumoroid Release and Analyses

2.2.1. Release of Tumoroids

After 48-h culture in the microwells, the channel layer was laterally shifted (slipped) relative to the microwell layer, thus, exposing the tumoroids in their enclosure to the air (**Figure 2**A, step 1). The microwell layer containing the tumoroids was gently washed with 1X Hank's Buffered Saline Solution (HBSS), while maintaining the tumoroids in the wells for subsequent imaging. The tumoroids were then released "on demand" from the microwells using forward-reverse pipetting of 5–10 µL of cell culture medium. A single tumoroid or up to 50 tumoroids per device (Figure 2A, step 2) was released and transferred into EKGel (Figure 2A, step 3) for long-term unconstrained culture in the chambered cell culture slide. Figure 2B illustrates an exemplary rod-shaped tumoroid released from ReSCUE and transferred to EKGel. The released tumoroids with other shapes are shown in Figure S5 (Supporting Information).

Upon release, all tumoroids maintained their structural integrity. The shape fidelity of the tumoroids during their formation and following the release from ReSCUE was assessed by comparing two morphological tumoroid properties – solidity and circularity – before and after the transfer into the EKGel. Solidity is a measure of the smoothness of the tumoroid contour (that is, its degree of concavity),[40] which is calculated as the ratio of the area enveloped by the total tumoroid contour to the total area in the regions bound by the corresponding convex contour of the tumoroid (Figure 2C). Solidity varies from 0 to 1, where 1 corresponds to tumoroids without concave features. Circularity is a measure of the tumoroid roundness and is calculated as the ratio of the tumoroid perimeter to the tumoroid area,[41] where zero circularity represents a line and a circularity of 1 represents a perfect circle (Figure 2C). Comparison of solidity and circularity values between the host wells and the respective tumoroids with disk, rod, and U shapes did not show a significant difference before and after their recovery from the ReSCUE platform, indicating a high fidelity in the growth and release of tumoroids with defined shapes (Figure 2D). More specifically, disk-, rod, and U-shape tumoroids had solidities of 0.98 ± 0.01, 0.97 ± 0.02, and 0.64 ± 0.04, respectively. The corresponding circularities were 0.88 ± 0.06, 0.54 ± 0.09, and 0.44 ± 0.07 (Figure S6, Supporting Information). These results indicate that differently shaped tumoroids can not only be identified visually by imaging, but also numerically by using morphological metrics.

2.2.2. Tumoroid Culture in an Unconstrained Environment

The tumoroids were cultured for 21 days in 100 µL of EKGel in the chambered cell culture slide (1 tumoroid per chamber), with the cell culture medium being replaced every 3 days. Tumoroid dimensions and shapes were examined at 7-day intervals. We selected tumoroids with disk, rod, and U shapes to study their growth in EKGel for 21 days following release. Another selected key geometric parameter, in addition to solidity and circularity, was the curvature of the tumoroid boundary, defined as the inverse of the radius of the osculating circle (the best circle approximating the curve) at the outer edge of the tumoroid. In the current study, positive and negative curvatures reflected a convex and a concave local shape (viewed from the tumoroid center). Disk-shaped tumoroids had consistently positive curvature; the curvature of rod-shaped tumoroids was high at the ends, but it gradually decreased to zero along the long edges of the rod. For U-shaped tumoroids, the ends and the outer curve had positive curvature, while the inner curve had a negative curvature. The transitions between the regions of positive and negative curvature involved inflection points with zero local curvature.

The growth and evolution of tumoroid shape following the release were characterized by analyzing their brightfield images over time (see experimental section for details). Over the 21-day culture period, tumoroids developed a densely packed core which was evidenced by the dark regions at the tumoroid center (Figure 2E). The tumoroids with different shapes displayed distinct growth patterns in unconstrained cultures. More specifically, disk-shaped tumoroids did not exhibit directional growth or the emergence of multicellular strands and retained their shape up to day 21 (Figure 2E, left column). In contrast, rod-shaped

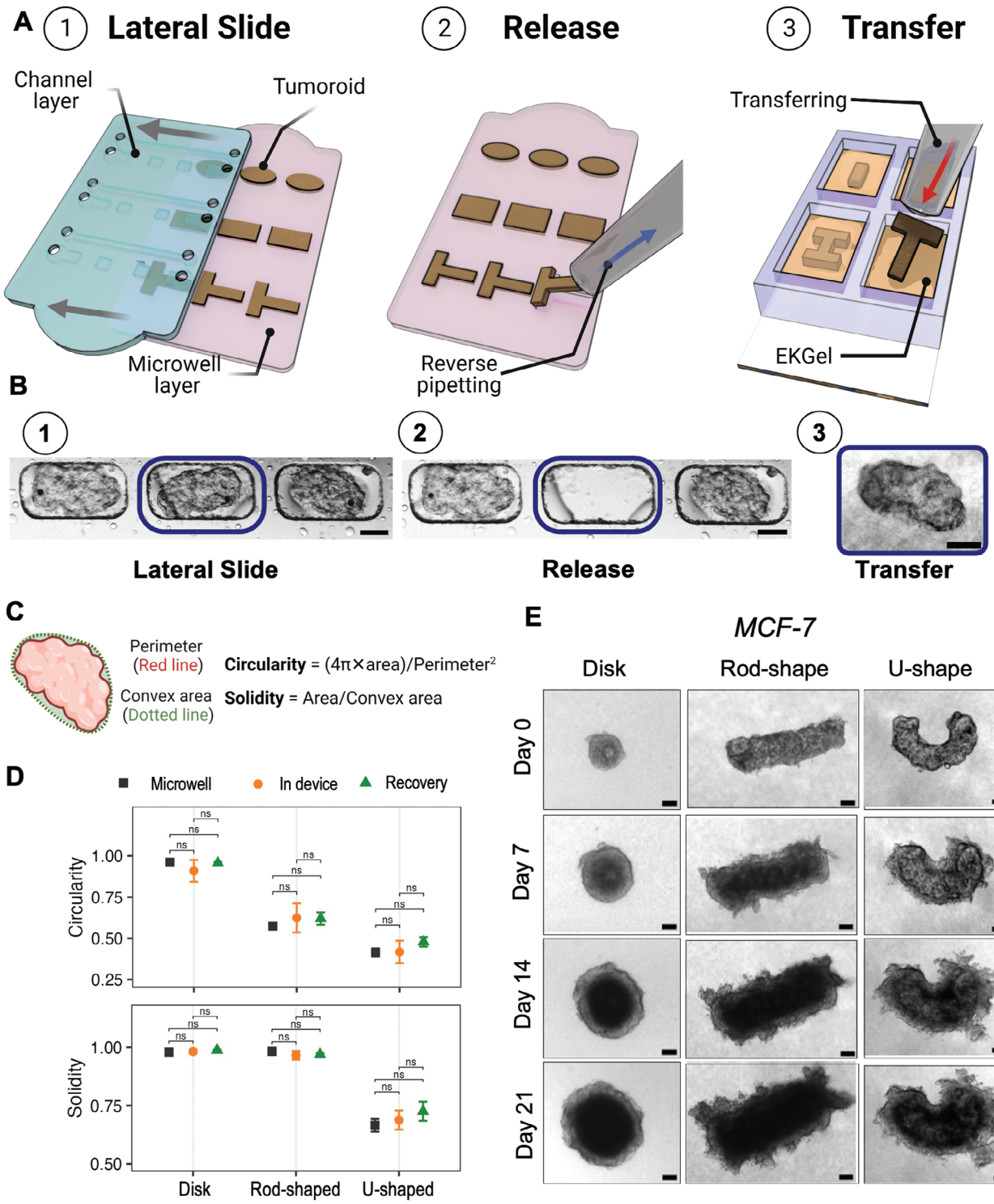

Figure 2. Release and transfer of tumoroids. A) Schematics of tumoroid release from the ReSCUE platform: (1) lateral sliding of the microwell layer (pink) to expose the tumoroids for removal from the ReSCUE. (2) Collection of selected tumoroids using forward-reverse pipetting (3) transfer of the selected tumoroids to the chambers containing EKGel. B) Brightfield images of MCF-7 tumoroids before and after the release: (1) a partial row of tumoroids after 48 h of cell culture. The tumoroid selected for release is marked with a frame. (2) Collection of selected tumoroids using a pipette, (3) Tumoroid transferred into a chambered cell culture slide containing EKGel for unconstrained culture. C) Definitions of circularity and solidity of tumoroids. D) Comparison of solidity and circularity of host microwells (*Microwell*), and different shape tumoroids after 48 h of cell culture in ReSCUE (*In device*) and after their release from the device (*Recovery*) using t-test for $n = 5$. The data are shown as mean ± std. dev. ($^{ns}p > 0.05$, $^{*}p < 0.05$, $^{**}p < 0.01$). E) Brightfield image of MCF-7 breast cancer disk-, rod-, and U-shaped tumoroids cultured in EKGel after releasing them from ReSCUE. EKGel with 1 wt.% a-CNCs and 2 wt.% gelatin was used for all the tumoroids. The scale bar is 200 µm.

tumoroids formed multicellular strands that were growing from the high positive curvature ends (Figure 2E, middle column). In U-shaped tumoroids, multicellular strands also preferentially appeared at the positive curvature regions, that is, at the rounded tips and the outer curved area, while the regions at the inner tumoroid region with negative curvature expanded to fill the area with the convex shape (Figure 2E, right column).

The versatility of the ReSCUE platform for the formation, release, and long-term culture of tumoroids with different shapes was further shown for non-malignant mammary epithelial MCF-10A cells (Figure S7, Supporting Information). The generation and release of MCF-10A tumoroids from the microfluidic device occurred with high fidelity. Experiments with MCF-10A tumoroids revealed that disk- and rod-shaped tumoroids formed a smaller number of strand-like multicellular structures, in comparison to U-shaped tumoroids, suggesting a stronger invasion of the latter. These results indicate that geometric cues impact the motility of non-malignant breast epithelial cells such as MCF-10A, in agreement with previous reports.[42,43]

2.3. Effect of Geometry on Growth of MCF-7 Tumoroids

The ability to release tumoroids in EKGel and subsequently monitor their growth in unconstrained conditions enabled a quantitative study of the global changes in their shape over a 21-day culture. We first analyzed the changes in the values of tumoroid solidity and circularity (**Figure** 3A,B, respectively). For disk-shaped tumoroids, the solidity and circularity remained close to 1.0. for the duration of the experiments. The solidity of rod-shaped tumoroids also stayed close to 1.0, however their circularity increased from 0.60 ± 0.03 to 0.73 ± 0.05 over time. For U-shaped tumoroids, the solidity increased from 0.78 ± 0.04 to 0.90 ± 0.04, and the circularity increased from 0.54 ± 0.05 to 0.71 ± 0.07. The time-dependent changes in the circularity and solidity of the tumoroids with different shapes are shown in Figure 3C.

Complementary to the global analysis of solidity and circularity, we studied site-specific changes in tumoroid shape by analyzing the changes in local curvature with increments of 70 µm. The local curvature C was defined and calculated at every location s along the tumoroid perimeter (Figure 3D), where s is the normalized position coordinate from the starting position with $s = 0$ (see details of the calculations in experimental section). With this definition of the local curvature, a closed contour (the tumoroid perimeter) has an end location ($s = 1.0$) that merges with the starting location ($s = 0$). As shown in Figure 3D, three ranges of curvature were defined: (i) positive curvature for $C > 1.5$ mm^{-1}, (ii) negative curvature for $C < -1.5$ mm^{-1}, and negligible curvature for -1.5 mm$^{-1} \leq C \leq 1.5$ mm^{-1}.

Figure 3E–G show the changes in local tumoroid curvature $C(s)$ over 21-day culture for disk-, rod-, and U-shaped tumoroids, respectively. While disk-shaped tumoroids maintained $C > 1.5$ mm^{-1} along the entire perimeter (Figure 3H), the shape of rod tumoroids changed noticeably over time, with local curvature C at the rod ends reducing by ≈20% (Figure 3I). Notably, the peaks corresponding to the rod ends retained their positions at $s = 0.25$ and $s = 0.75$ over time (Figure 3I). For U-shaped tumoroids, the peaks in curvature (located also at $s = 0.25$ and $s = 0.75$) were reduced in value by almost 35%, while the wells located at $s = 0.5$ were reduced by 57% (Figure 3J). The results for rod- and U-shaped tumoroids indicate a significant temporal reduction in the absolute values in negative and positive curvatures. These changes may have originated from the effect of interfacial tension reducing at the interface between the tumoroids and the surrounding EKGel.[44] Furthermore, a significant reduction in the absolute value of the negative curvature for U-shaped tumoroids may occur due to the additive effects of actomyosin contractility and cell crawling, leading to a faster expansion of cells in these regions.[45,46] Notably, despite all the changes in the geometric tumoroid characteristics over 21-day unconstrained growth, their pre-defined shapes arising from initial microwell confinement were largely preserved.

The ability to recover tumoroids from ReSCUE enabled the study of cell proliferation in different tumoroid regions. To examine local cell proliferation in the regions with a broad spectrum of curvature values, we selected the U-shaped tumoroids, as they contain regions with both positive and negative curvatures. Representative confocal microscopy images in Figure 3K,L show a U-shaped tumoroid stained with the proliferation marker Ki-67 on Day 1 and 21, respectively. On Day 1, proliferative cells were uniformly distributed across regions with different curvatures (Figure 3K-1,K-2). By Day 21, the proliferative cells accumulated in the positive curvature regions, and multicellular strands extended specifically from these regions (Figure 3L-1). In contrast, cells exhibited a lower level of Ki-67 expression in the regions with negative curvatures (Figure 3L-2). The dark region in the tumoroid core appeared on Day 21 and was attributed to the restricted diffusion of Ki-67 and limited light penetration in the core of densified tumoroids in the confocal microscopy imaging and presence of necrosis in the central region (Figure S8, Supporting Information).[47] Overall, the distribution of Ki-67-positive cells implied that cells in the regions with positive curvature were more proliferative, leading to the formation of multicellular strands.

2.4. Growth of Patient-Derived Tumoroids

Next, ReSCUE was used for the growth and release of PDOs generated from two breast cancer patient-derived organoid (PDO) models, one metastatic and the other primary (DCXBTO.58 and BPTO.95, respectively) (Table S1- Supporting Information). A strategy similar to tumoroid formation was used to generate cell-laden droplets with different shapes. Disk-, rod-, and U-shaped PDOs (DCXBTO.58) formed in the ReSCUE after 96 h of continuous perfusion of the cell culture medium using gravity-driven flow. The formation of cell-cell junctions was confirmed by staining PDOs with E-cadherin antibody (**Figure** 4A), while staining of F-actin and DAPI revealed the spreading of actin filaments in the cell cytoskeleton and cell nuclei in the PDOs, respectively. Following a 96-hour cell culture period in ReSCUE, the PDOs were released, transferred into EKGel in the chambered cell culture slide, and cultured for 21 days. The brightfield PDO images shown in Figure 4B revealed that up to Day 21 the PDOs retained their pre-designed shapes, although the average curvature at the tips of rod- and U-shaped PDOs was reduced.

The role of shape in PDO growth was examined by calculating the local changes in PDO curvature, as described in Materials and

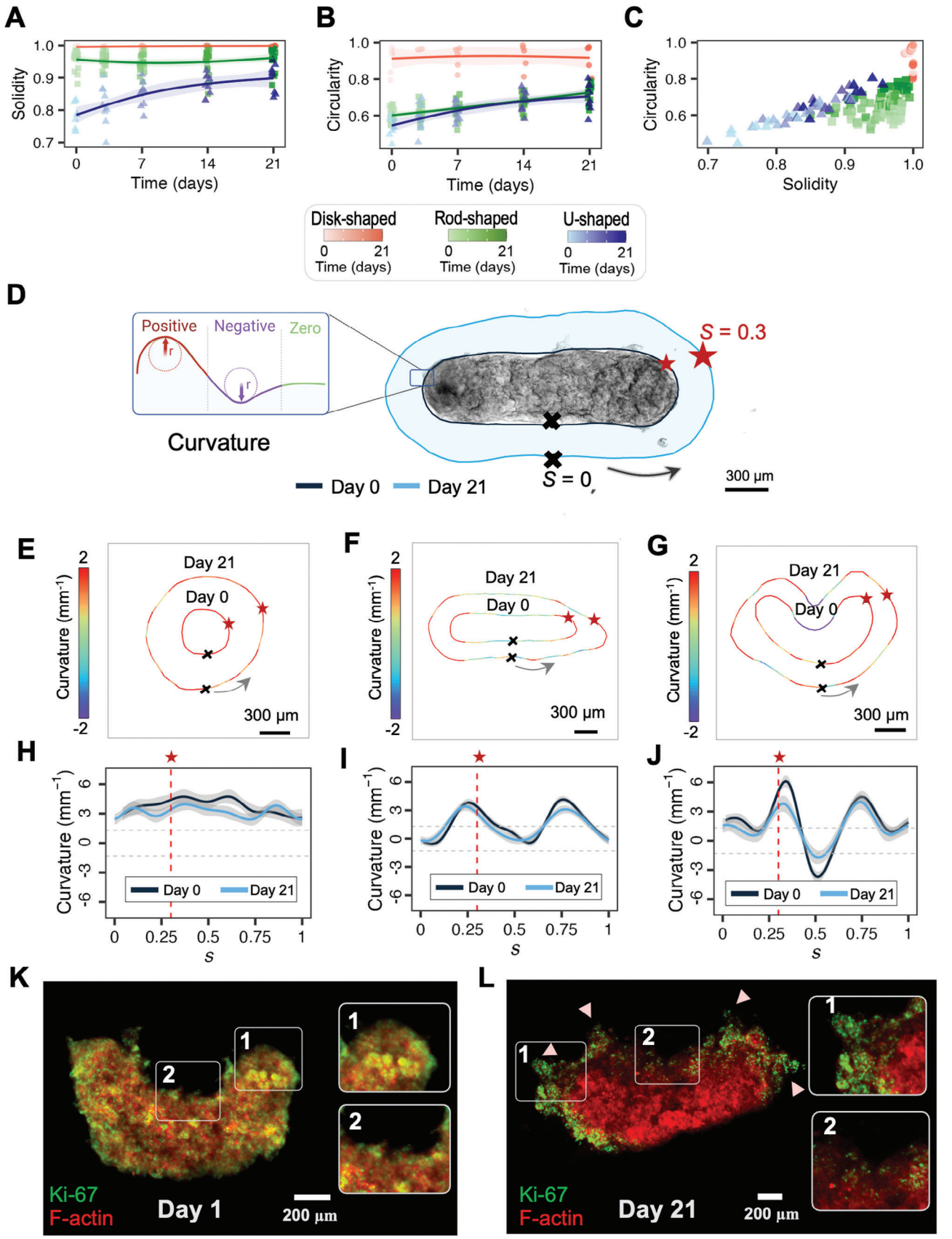

Methods. Figure 4C,F show that after 21 days of unconstrained culture, disk-shaped PDOs maintained $C > 1.5\ mm^{-1}$ along the entire perimeter, which was indicative of a uniform PDO expansion without directional growth. For the rod-shaped PDOs, the curvature values for two maximum positive peaks at the rounded ends decreased by almost 40%, while the curvature value along the long PDO side remained constant (Figure 4D,G). The positions of the maximum positive peaks at $s = 0.25$ and $s = 0.75$ remained constant (Figure 4G). For U-shaped PDOs, the value of C for two peaks at $s = 0.25$ and $s = 0.75$ decreased by ≈33% and the trough of $C = -4.5 \pm 0.3\ mm^{-1}$ located at $s = 0.5$ reduced by 48% (Figure 4E,H). The circularity and solidity of the PDOs with different shapes increased (except the solidity of disk-shaped PDOs) (Figure S9, Supporting Information). Overall, the examination of the geometry of rod- and U-shaped PDOs showed that the positions of the maximum positive and negative curvatures were preserved. The average local curvature along the PDO perimeter reduced, aligning with the observations made for the MCF-7 tumoroids.

The role of PDO shapes in their expansion rate was examined by analyzing the increase in their area over 21 days. Figure 4I displays a similar linear time-dependent increase in the areas of PDOs with different shapes. To explain this trend, for each PDO shape, we determined the fraction of the regions with positive, negative, and zero curvature in the PDO perimeter. Figure 4J shows that in disk-shaped PDOs over 85% of the perimeter displayed moderate positive curvature, while in rod-shaped PDOs, only 45% of the perimeter had higher positive curvature regions. For U-shaped PDOs, ≈50% had high positive curvatures, with the rest of its perimeter exhibiting negative and zero curvature. Thus, while higher positive curvature regions showed faster growth, the slower expansion of cells in the areas with negative and zero curvature counterbalanced this effect in rod- and U-shaped PDOs, which resulted in similar overall growth of PDOs with all three shapes.

To examine the role of curvature on the local cell proliferation, we performed Ki-67 staining of U-shaped PDOs (Figure 4K,L). On Day 1, the proliferative cells were localized close to the PDO periphery, with a lower level of Ki-67 expression in the regions with negative curvature (Figure 4K-1,K-2). After 21 days, this trend became stronger, that is, the proliferative cells localized strictly at the PDO/gel interface, and high Ki-67 expression was observed in the higher curvature PDO ends (Figure 4L-1,L-2). Multicellular strands of proliferative cells grew solely from the locations with high positive curvature (Figure 4L-1). The difference in growth patterns of differently shaped PDOs (and tumoroids) can be attributed to cell density.[48,49] More specifically, cancer cells are densely packed and constrained in high-positive curvature regions of rod- and U-shaped PDOs, in comparison with their disk-shaped counterparts. Evacuation of PDOs from ReSCUE to an unconstrained gel environment resulted in a higher cell density and a higher growth rate in the high-curvature regions, thereby recapitulating malignant tumor progression that occurs in vivo.[50]

To explore in greater detail the shape-growth relationship for PDOs, we evaluated histological sections and immunohistochemical stains. After 21-day growth in the unconstrained EKGel, the released rod-shaped PDOs were fixed with formalin, paraffin-embedded, sectioned in samples with 4–5 µm thickness, and stained with hematoxylin and eosin (H&E), Ki-67, and E-cadherin. The H&E staining of rod-shaped PDO (Figure 4M, left panel) showed a higher cell density in the regions with positive curvatures. In addition, the Ki-67 staining (Figure 4M, middle panel) shows a higher number of proliferating cells at the tips of rod-shaped PDO, which aligned with the results of immunofluorescence staining (Figure 4K,L). Staining with E-cadherin showed that cell-cell junctions formed in the entire rod-shaped PDO (Figure 4M, right panel). Notably, a larger number of protrusions in Figure 4M, right panel were observed in the PDO regions with positive curvature, compared to the regions with zero curvature. To further compare PDO growth in the regions with different curvatures, we developed a theoretical model, based on the image processing algorithm (Note S13, Supporting information). The modeling results showed that the overall growth of tumoroids and PDOs was significantly higher in the regions with positive curvature, compared to the regions with zero or negative curvatures (Figure S14, Supporting information), which was consistent with experimental results.

2.5. Effect of Curvature on Cancer Cells Behavior

We stained the cells with Hematoxylin and Eosin (H&E) for cell morphology, Ki-67 for proliferative cells, and E-cadherin for cell-cell junctions. To determine how cells respond to PDO curvatures, we used a commercially available image-processing algorithm HALO. We first quantified cell density in various regions with different curvatures in PDOs. The results of H&E staining showed higher cell density in regions with positive curvature compared to regions with negative or zero curvature. Next, we investigated the proliferation of cells in the PDOs with different shapes. In disk-shaped PDOs with uniform curvature, Ki-67-positive cells were distributed without any spatial preference along the PDO periphery. In contrast, in rod- and U-shaped PDOs a greater number of proliferative cells localized in the regions with positive curvature, which aligned with the results of immunofluorescence staining (Figure 4K,L). We also examined the shape of cells using E-cadherin staining. **Figure 5C** shows that in

Figure 3. Effect of geometry on tumoroid growth. A,B) Changes of the circularity and solidity of disk-, rod-, and U-shaped tumoroids after 21-day culture. The shaded regions show the confidence interval with standard deviation ($n = 5$). C) Temporal trend in circularity and solidity of disk-, rod-, and U-shaped tumoroids after 21-day culture. ($n = 5$). D) Representative schematic of the analysis of curvature of the tumoroid. The range of curvatures in the analysis was defined as positive ($C > 1.5\ mm^{-1}$), negative ($C < -1.5\ mm^{-1}$), and zero ($-1.5\ mm^{-1} < C < 1.5\ mm^{-1}$), using an incremental step of 70 µm. The black cross represents the starting point ($s = 0$) on the tumoroid perimeter in measurements of its curvature and the red star indicates $s = 0.3$, or 30% of the tumoroid perimeter. The scale bar is 300 µm. E–G) The variation in the curvature of the representative disk- (E), rod- (F) and U-shaped (G) tumoroids on days 0 and 21 H-J) Curvature profile of the disk-, rod-, and U-shaped tumoroids along their perimeters on days 0 and 21. The shaded regions show the confidence interval with standard error ($n = 5$). K&L) Immunostaining of the tumoroids on Day 1 and 21 of unconstrained growth in EKGel with F-Actin (Alexa Fluor 568 Phalloidin, red) and Ki-67 (rabbit monoclonal antibody, green). Scale bars are 200 µm.

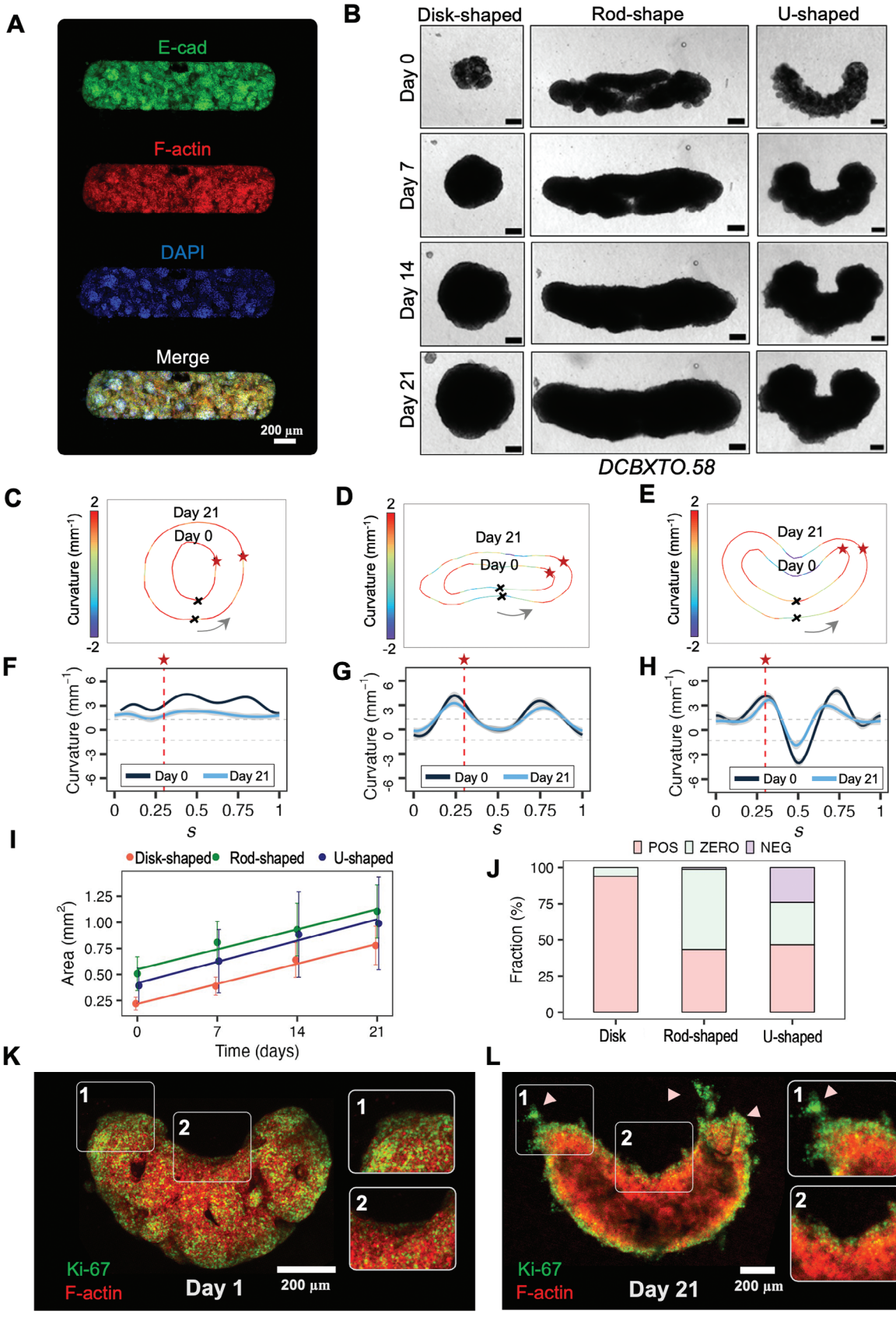

the regions of positive curvatures in U-shaped PDO, cells formed looser cell-cell junctions in contrast to the tight junctions in the regions with negative and zero curvature. Cell invasion was particularly evident at the tips of the rod-shaped PDOs, where cells formed multiple protrusions. Notably, such protrusions were not observed in the PDO regions with zero and negative curvature.

To further examine curvature-dependent cell behavior, we divided U-shaped PDOs into three regions exhibiting positive, zero, and negative curvatures, as shown in Figure 5D. In the positive curvature regions cells formed denser structureshour (Figure 5E) and were more proliferative based on the expression of Ki-67, (Figure 5F). Using E-cadherin immunohistostaining, we examined the shapes of nuclei and cell-cell distances. The results showed that cells in regions with positive curvature (near the PDO boundary) have a less round shape compared to cells localized in regions with negative curvature, thus suggesting a more invasive behavior in the positively curved regions (Figure 5G).[51] In the regions with different curvatures, cell-cell junctions did not change as shown in Figure 5H. These findings suggest that PDO curvature influences cell density, proliferation, and nuclei shape, but does not significantly influence cell-cell junctions between cancer cells in U-shaped PDOs. Further studies are needed to explore the mechanisms underlying these observations to determine the broader implications for tumor invasion.

3. Discussion and Conclusions

The ReSCUE platform enables the efficient formation of uniformly sized tumoroids and PDOs with different morphologies, as well as their subsequent high-fidelity release from the microfluidic device and post-recovery long-term culture in an unconstrained environment comprised of a 3D biomimetic hydrogel. This capability was demonstrated for non-malignant MCF-10A breast epithelial, and malignant MCF-7 breast cancer cell lines and two independent PDO breast cancer models (DCXBTO.58 and BPTO.95), showing the robustness and versatility of the platform. Importantly, tumoroids and PDOs with dimensions on the order of hundreds of micrometers were formed within only 2 and 4 days, respectively. Tumoroids and PDOs were released from ReSCUE either all at once, or by targeted identification, thereby allowing post-release culture and analyses to examine tumor growth. In the current work, we explored the impact of tumor shape on collective cell invasion, but the utility of ReSCUE could naturally be extended to study the impact of other perturbations, e.g., drug treatment or cell co-culture on macroscopic tumor structure in a controllable in vitro environment.

The ability to grow and release tumoroids and PDOs enabled a study of their shape-dependent growth kinetics and invasion. After 21-day culture, they preserved their original shape, although changes in circularity, solidity, and curvature revealed faster tumoroid and PDO expansion in the regions with higher positive curvature. In such regions, cancer cells formed densely packed structures. The results of histological studies revealed that proliferating cancer cells were enriched in these locations, with possible formation of leader cells in the high curvature regions. For example, in U-shaped PDOs, cell migration was observed toward the regions with positive curvature. The difference in the cell invasion behavior can be attributed to the reorganization in the cell cytoskeleton, leading to the formation of protrusions in positive curvature regions and contractile actomyosin cables in negative curvature regions. Further research is needed to discover the underlying mechanisms of the difference in cell invasion in the regions with positive and negative curvatures. Unraveling the underlying mechanisms responsible for this behavior would require further investigation of the signaling pathways associated with this distinct invasive behavior in high curvature regions of PDOs. Staining for molecular markers such as N-Cadherin,[52] vimentin,[52] TWIST1,[53] ZEB1,[54] and Snail[54] may provide more insight into the mechanism of this effect. Lineage tracing and RNA-sequencing would enable refinement of the concept of leader cells and establish a comprehensive framework for understanding the effect of PDO morphology on leader-follower organization. While these mechanisms are beyond the scope of this work, they provide an example of the biological or therapeutic concepts that are addressable with the use of the ReSCUE platform.

Another important aspect of collective invasion is forces applied to cells, where migrating cells experience shear and normal stress.[45] It has been shown that leader cells tend to minimize the shear stress while maximizing the normal stress by exerting forces through pulling and orienting the follower cells.[24,25,55] Our findings suggest that cells at the positive curvature locations exert forces to propel themselves forward, while cells at the negative curvature regions may experience compression force, due to the crowding or resistance from surrounding cells or matrix. Further experiments are necessary to decipher the mechanobiological signals involved in collective cell migration.

Tumor shape is crucial in the clinical cancer treatment decision-making process, as it serves as one of the indicators of malignancy in medical imaging and radiomics.[56–59] For instance, non-spherical or irregularly shaped tumors in lung cancer often indicate a higher malignancy probability than spherical ones.[60,61] The utilization of ReSCUE platform provides the capability to generate tumoroids and PDOs with controlled geometric characteristics (circularity, solidity, and curvature), thus, paving the way to comprehensive studies of the relationship between tumor shape and growth treatment in vitro. For all cell types, an increase in circularity and solidity of growing tumoroids and PDOs was observed. The local curvature analysis of the tumoroids and PDOs over time demonstrated an overall reduction

Figure 4. Generation, release, and post-culture of breast cancer patient-derived organoids (PDOs) with different shapes. A) Immunostaining of rod-shape and U-shape PDOs formed after 96-h cell culture with F-Actin (Alexa Fluor 568 Phalloidin, red), E-Cadherin (Rabbit Monoclonal Antibody, green), and DAPI (blue). The scale bar is 200 µm. B) Brightfield image of PDO disk-, rod-, and U-shape geometries, which were released from ReSCUE and cultured in EKGel with unconstrained conditions. (C-E) The variation in the curvature of a representative disk-shaped C), rod-shaped D), and U-shaped E). F-H) Curvature profile of the disk-, rod-, and U-shaped PDOs along their perimeters on days 0 and 21. The shaded regions show the confidence interval with standard error ($n = 5$). I) Increase in the area of PDOs over 21-day unconstrained growth in EKGel ($n = 5$). The data are shown as mean ± std. dev. for all PDOs. J) Fraction of positive, negative, and zero curvature regions in PDOs with different shapes on Day 0. K, iL) Immunostaining of PDOs on Day 1 and 21 with F-Actin (Alexa Fluor 568 Phalloidin, red) and Ki-67 (rabbit monoclonal antibody, green). Scale bars are 200 µm.

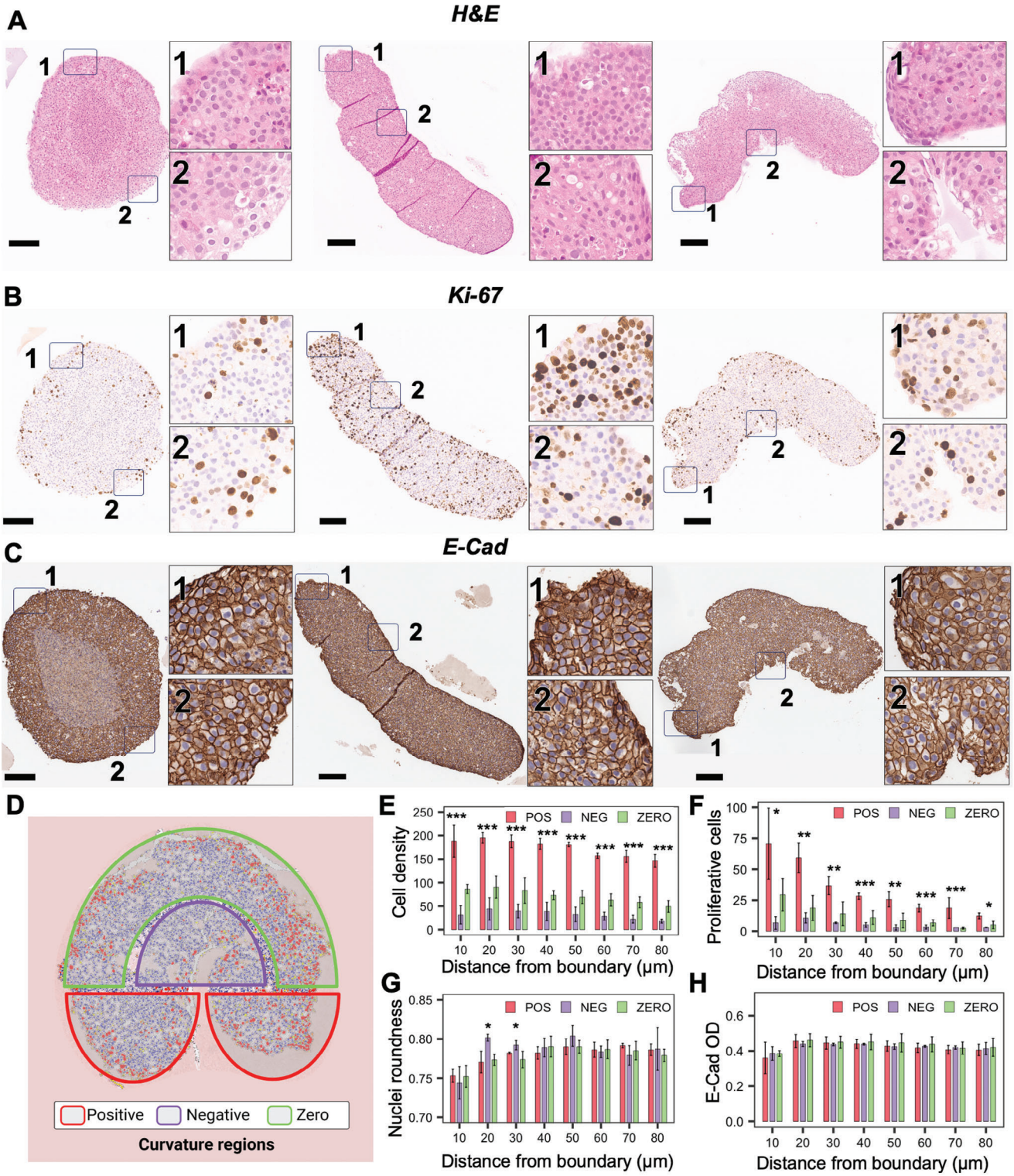

Figure 5. Immunohistochemistry analysis of disk-, rod, and U-shape PDOs after 21 days of post-culture. A) Hematoxylin and eosin (H&E) staining of PDO cytomorphology. B) Ki-67 staining for localization of proliferative cells. C) E-cadherin staining for characterization of cell-cell junctions. Scale bars are 200 μm D) Schematic of positive, negative, and zero curvatures of three different curvature regions of U-shaped PDOs E-H) Cell density, number of proliferative cells, cell nuclei roundness, and cell-cell junction, plotted as a function of the distance from the PDO boundary in regions with different curvature of U-shaped PDO after 21 days of culture under unconstrained conditions ($n = 5$). The data are shown as mean ± std. dev. ($^{ns}p > 0.05$, $^{*}p < 0.05$, $^{**}p < 0.01$).

in local curvature fluctuations along their perimeter, suggesting the trend for the reduction of the interfacial area of the tumoroids and PDOs with the surrounding hydrogel. Furthermore, we found that positive curvature significantly enhanced local cell migration for MCF-7 tumoroids and PDOs, with the most significant effect in rod-shaped PDOs. These differences in growth and invasion behavior underscore the importance of using patient-derived models which are more representative of the native tumor microenvironment than commercial cell lines.

Importantly, the transition from 2D-shaped cell aggregates to 3D spheroids and PDOs is essential to unraveling cellular behavior under physiologically relevant conditions. While 2D micropatterning allows the guidance of microtissue by controlling cell boundaries, the transition to 3D shapes more accurately represents the in vivo environment. Therefore, such transition not only enhances our understanding of the behavior of cells, but also contributes to regenerative medicine by enabling the formation of functional tissues and organs. The effect of tumor shape on tumor growth, and ultimately, patient survival outcomes has recently garnered significant attention. For example, imaging tumors of different shapes has enabled risk prediction for lung cancer in various patients.[62] In another study, the shapes of breast cancer tumors obtained through MRI imaging were used to classify the degree of invasion.[56] In this study, breast cancer tumors were categorized into four distinct shapes: spherical, discoidal, segmental, and irregular. It was found that only 19% of the 83 breast cancer tumors examined were spherical. Another study, based on 52 patients with squamous cell carcinoma, showed that tumor shape is associated with perineural invasion.[63] These studies highlight that well-defined spherical tumors exhibited nearly half the incidence of invasion compared to irregularly shaped tumors. We envision that the ability to form differently shaped PDOs enables studies of the role of structural irregularities in solid tumors and in general, cancer progression. In this context, the ReSCUE platform empowers the formation, release, and characterization of 3D tissues from patient-derived cells, offering a valuable tool for in-depth analysis of cancer invasion and advancing fundamental cancer research and drug screening. For example, the macroscopic tumoroids and PDOs generated in ReSCUE can find particular utility in evaluating the response of heterogenous models to therapy, including the determinants of individual cell fate and the consequent repopulation or reorganization occurring in the absence of tumor eradication. We envision that this platform may be particularly relevant for the evaluation of the rapidly expanding class of antibody-drug conjugates (ADCs), whose activity is governed by cell-intrinsic and neighborhood effects.

The applications of ReSCUE can extend beyond cancer research, e.g., for the formation of 3D muscle tissues as biocurators for microrobots,[64] engineered human cortical, forebrain, and bladder assembloids,[65,66] and organoid tissue engineering with a middle-out approach achieved due to precise spatiotemporal control of cell niche.[67] In addition, the engineered human assembloids or organoids of different shapes may also be used in multi-tissue micro-physiological systems (MPS) and linked "organ-on-a-chip" platforms for drug screening or disease development studies. In cancer research, the impact of tumor shape on radiation therapy is also a critical area of research for optimizing radiation dosing and choosing the appropriate tumor margin.[56,68]

4. Experimental Section

Fabrication and Assembly of ReSCUE: *Fabrication of the ReSCUE Platform*: ReSCUE was fabricated in poly(methyl methacrylate) sheets (P/N: 8560K171, 1/16'', McMaster-Carr, USA). The MF device consisted of two sheets (layers) and was designed using computer-aided design software Fusion 360 (Autodesk Inc, USA). The design of each layer is provided in Supporting Information. The tool paths and set parameters were generated using Fusion 360 and transferred as G-code files to a 3-axis milling machine (PCNC770, Tormach, USA). The poly(methyl methacrylate) sheets were affixed to the machining table using double-sided tape (Grand & Toy, Canada). Next, the CNC machine executed the G-code to micromill the sheets. Uncoated carbide square endmills with diameters of 0.01'' (MasterCut P/N 207-104), 0.015'' (P/N: 11 101 500, TuffCut – M.A. Ford), 1/32'' (P/N: 209-202-1, MasterCut), or 5/64'' (P/N: 103–783, Mfr: SOWA). The sheets were cleaned by ultrasound sonication in Milli-Q grade deionized water (DI, 18.2 MΩ cm resistivity) and sterilized by spraying 70% ethanol.

Assembly of the ReSCUE Platform: Prior to assembly, a hydrophobic coating (Rain-X, ITW Global Brands, USA) was applied to the sheets, and they were dried at 65 °C for 5 min. Subsequently, for sterilization, the layers were exposed to UV irradiation (254 nm, 345 μW cm^{-2}) for 20 min. Next, silicone oil (20 cSt, Sigma-Aldrich, USA) was applied to both sheets to prevent possible leakage in the ReSCUE and act as a lubricant during the sliding, The sheets were superimposed under a stereoscope using the alignment-helping marks, clamped, and oil excess was removed. Alignment features at the corners of the topographically patterned sheets (layers) assisted in ReSCUE assembly.

Cell Culture: MCF-7 cells and human dermal fibroblasts (hDFs) were cultured in the incubator at 37 °C with a constant supply of 5% CO2 in T75 flasks with 10 mL of medium consisting of DMEM, supplemented with 10% (v/v) fetal bovine serum, 1% (v/v) penicillin/streptomycin. MCF-10A was cultured in the incubator (37 °C and 5% CO2) in T75 flasks with 10 mL medium consisting of DMEM/F12 with 5% (v/v) horse serum, (20 ng mL^{-1}) EGF, (0.5 mg mL^{-1}), hydrocortisone, 0.1% (v/v) insulin, and 1% (v/v) penicillin/streptomycin. For cell passaging or preparing the cells for MF experiments, they were detached from T75 flasks using 3 mL trypsin-EDTA solution for 10 min at 37 °C, followed by the addition of 7 mL of complete cell culture medium. The cell suspension was centrifuged at 184 g at 20 °C for 3 min. For cell passaging, the cell pellet was re-suspended in 1 mL of complete cell culture medium, and 300 μL of the cell suspension was transferred into a new flask containing 10 mL of the complete cell culture medium.

Patient-Derived Cancer Organoids Culture and Passage: Patient tumor tissue was obtained with informed patient consent and used for cell collection in accordance with approved protocols from the UHN Research Ethics Board (06–196, 17—5518, and 14–8358). The tumors were minced and digested in Advanced DMEM/F12 supplemented with GlutaMAX, HEPES, and antibiotic-antimycotic (ADF+++) along with 500 μg mL^{-1} Liberase TH. After gentle rocking at 37 °C for 1 h, the samples were further dissociated by pipetting. ADF+++ was added to reach a final volume of 13 mL, followed by centrifugation at 400 g for 15 min at 4 °C. The resulting cell pellet was resuspended in TrypLE Express and incubated at 37 °C for 15 min. Subsequently, ADF+++ was added to a final volume of 13 mL, and the sample was passed through a 100 μm cell strainer. After centrifugation at 300 g for 5 min at 4 °C, the cell pellet was treated with Red Cell Lysing Solution on ice. ADF+++ was added to increase the volume to 10 mL, and cells were centrifuged at 300 g for 5 min at 4 °C. Previously generated and characterized organoids were seeded, grown, and expanded in EKGel for use in the RESCUE experiments.

Dissociated organoids were resuspended in EKGel precursors at a density of 100 cells μL^{-1}. The cell-laden mixture was then plated in a 24-well plate at a volume of 300 μL per EKGel per well. Following a 2-hour well plate incubation in the incubator at 37 °C to allow for gelation, 750 μL of breast

organoid medium was overlaid on each well. The medium was changed every 3–4 days, and PDOs were passaged every 14 days. For passaging, the medium in each well was replaced with 1 mL of TrypLE Express. the PDO was recovered from EKGel by pipetting up and down with a P1000 pipette. The resulting cell suspension was centrifuged at 300 g for 5 min and the supernatant was removed. The PDOs were then resuspended in fresh TrypLE Express, returned to wells, and incubated at 37 °C, with manual shearing every 10 min, until they dissociated into individual cells. The dissociated cells were transferred into a 15 mL falcon tube, and TrypLE was neutralized by adding ADF+++. After centrifugation at 300 g for 5 min, the supernatant was removed, and cells were counted and resuspended in the EKGel precursor suspension.

Cell Culture and Formation of Tumoroids and PDOs using ReSCUE: MCF-7 cells (2.0×10^5 cell μL^{-1}), MCF-10A (2.0×10^5 cell μL^{-1}) or patient-derived cells (patient line 1: ER-/PR-/HER2 and patient line 2: ER-/PR-/HER2) (1.5×10^5 cell μL^{-1}) were mixed the suspension of the hydrogel precursors, EKGel. The tumoroids were generated from a suspension of breast cancer cells in an aqueous mixture of EKGel precursor, that is, aldehyde-functionalized cellulose nanocrystals (a-CNCs) and gelatin. The reaction between the aldehyde groups of a-CNCs and the primary amine groups of the lysine residues in gelatin led to the formation of the hydrogel with 1 wt.% a-CNCs and 2 wt.% of gelatin (later in the text referred to as EKGel).[69] Subsequently, this suspension was introduced in the MF device with 6 loading channels, each accommodating 7 µL of the suspension. Next, the cell-laden droplets were formed by laterally sliding the microwell layer with respect to the Channel Layer. Following incubation of the device for 2 h at 37 °C for gel formation, the cell culture media was perfused through the device using gravity-driven flow. The gravity-mediated flow was achieved by placing a pipette tip filled with 300 µL of the cell culture medium at the inlet and an empty pipette tip at the outlet of the MF device and positioning the entire device on a rocker platform (Ohaus SHRK04DG, TEquipment, USA). The platform was set to rock at a 15° tilting angle and a tilting speed of 1 rpm (1 full-rocking motion per min). In 2–4 days (depending on the cell type), the cell-laden microgels transformed into tumoroids or PDOs with the shape determined by the microwell geometry.

Cell Viability: To assess cell viability within the tumoroids and PDOs, the cells were stained with 2.0 µM calcein-AM solution (Sigma-Aldrich, USA) to visualize live cells (green fluorescence) and 6.0 µM propidium iodide solution (BioShop, Canada) to visualize dead cells (red fluorescence). A staining solution was perfused into the ReSCUE at 37 °C using gravity-driven flow on a rocker platform at a 15° tilting angle and 1 rpm tilting speed. After 1 h perfusion of the staining solution, the cells were visualized using a Nikon Eclipse fluorescence microscope. Live cells were visualized using excitation wavelengths of 480/30 nm and emission wavelengths of 535/45 nm. Dead cells were examined using excitation wavelengths of 540/25 nm and emission wavelengths of 605/55 nm.

Image Acquisition and Data Processing: During the 21-day culture period, brightfield images of tumoroids and PDOs were captured every 7 days using the Nikon Ti Eclipse microscope. The tumoroid and PDO boundaries were analyzed manually using ImageJ software (National Institutes of Health, USA), and the boundaries were exported using their coordinates. To facilitate data processing, a Python script was developed (https://github.com/yakavetsiv/curvature.git).

The perimeter of tumoroids and PDOs was generated as a collection of coordinates (X, Y) with a distance between adjacent points of 70 µm. The selection of the increments for analyzing the local curvatures along the tumoroid perimeter was determined by imaging resolution and the signal-to-noise ratio. In the analysis of curvature of tumoroids and PDOs, the initial point for the analysis was standardized to be the middle pixel (X_{middle}) of the lowest part of (Y_{min}) of the perimeter of the tumoroid and PDO. The coordinates were further smoothened using the spline function.[70] The analysis of the circularity and solidity of tumoroids and PDOs was carried out using the same method.

PDO Histology: The cell culture medium was removed from the culture chambers. Next, the tumoroids or PDOs were transferred into cryomolds (Andwin Scientific CRYOMOLD, Thermo Fisher Scientific, USA) containing liquid HistoGel (Thermo Fisher Scientific, USA). After the mixture was solidified, it was transferred to a histology cassette (Epredia Cassette, Thermo Fisher Scientific, USA). Subsequently, it was immersed in 10% buffered formalin to fix the cells. Paraffin embedding and immunohistochemistry were performed by DDP-AMPL at the University Health Network (UHN, Canada).

Immunofluorescence Staining: Tumoroids and PDOs were washed with 1× HBSS twice to remove the cell culture medium and fixed with 300 µL of 5.0 wt.% formalin for 30 min. The fixed tumoroids and PDOs were washed three times with 500 µL solution of 0.1-M glycine in HBSS, which was subsequently replaced with 300 µL of 0.5 vol% solution of Triton-X in 1× HBSS for 20 min to permeabilize the cells. The tumoroids and PDOs were then washed three times with 500 µL of immunofluorescence solution (0.05 wt.% NaN3, 0.1 wt.% bovine serum albumin, 0.2 vol% Triton-X-100, and 0.05 vol% Tween-20 in HBSS). A primary blocking solution (10 wt.% goat serum in immunofluorescence solution) was then added to the tumoroids or PDOs, incubated for 90 min, and subsequently replaced with 300 µL of antibody solution. For F-actin and E-cadherin staining, AlexaFluor 488 E-Cadherin rabbit monoclonal antibody (Cell Signaling Technology) and AlexaFluor 568 Phalloidin (Life Technologies) were diluted at 1:800 dilution in the primary blocking solution. For F-actin and Ki-67 staining, AlexaFluor 488 Ki-67 rabbit monoclonal antibody and AlexaFluor 568 Phalloidin (Life Technologies) were diluted at the volume ratio of 1:800 with the primary blocking solution. The stained tumoroids and PDOs were then incubated overnight at 4 °C. To stain cell nuclei, DAPI (Hoechst solution) was introduced into the ReSCUE for 20 min.

Statistical Analysis: All data in the Results section are presented as mean ± standard deviation unless otherwise specified. Statistical significance was determined using student's t-test or ANOVA, and p-values < 0.05 were considered significant. All the student's t-tests and ANOVA were performed in R software. For the measurements of circularity and solidity of the tumoroids and PDOs, $n = 10$ for each shape. For curvature and growth analysis measurement, $n = 5$ for each PDO and MCF-7 tumoroid, unless otherwise specified.

Supporting Information

Supporting Information is available from the Wiley Online Library or from the author.

Acknowledgements

S.K. and I.Y. contributed equally to this work. The authors acknowledge A. Gevorkian for their contribution in the initial conceptualization of the study, and Mitchell J. Elliott for the consultation on patient-derived organoids. Some figure panels are created with BioRender.com. This work was supported by the following financial support: Ontario Graduate Scholarship (SK), Barbara and Frank Milligan Fellowship (SK), Natural Sciences and Engineering Research Council of Canada CREATE Training Program in Organ-on-a-Chip Engineering and Entrepreneurship (SK, IY), Precision Medicine Initiative (IY), University Health Network Fellowship #PRMUHN2022-006 (IY), Natural Sciences and Engineering Research Council of Canada #RGPIN-2019-5885 (EWKY), New Frontiers in Research Fund (EK), Foundation for Innovation/Ontario Research Fund #36 442 (EK).

Conflict of Interest

The authors declare no conflict of interest.

Data Availability Statement

The data that support the findings of this study are available from the corresponding author upon reasonable request.

Keywords

cancer, microfluidics, narrative engineering, organoids, spheroids, tissue engineering

Received: July 20, 2024
Revised: August 15, 2024
Published online:

[1] T. Takebe, J. M. Wells, *Science* **2019**, *364*, 956.
[2] J. Drost, H. Clevers, *Nat. Rev. Cancer* **2018**, *18*, 407.
[3] H. Clevers, *Cell* **2016**, *165*, 1586.
[4] D. Tuveson, H. Clevers, *Science* **2019**, *364*, 952.
[5] G. Rossi, A. Manfrin, M. P. Lutolf, *Nat. Rev. Genet.* **2018**, *19*, 671.
[6] Z. Zhao, X. Chen, A. M. Dowbaj, A. Sljukic, K. Bratlie, L. Lin, E. L. S. Fong, G. M. Balachander, Z. Chen, A. Soragni, M. Huch, Y. A. Zeng, Q. Wang, H. Yu, *Nat Rev Methods Primers* **2022**, *2*, 94.
[7] P. Wörsdörfer, T. I., I. Asahina, Y. Sumita, S. Ergün, *J Neural Transm* **2020**, *127*, 1569.
[8] C. R. Marti-Figueroa, R. S. Ashton, *Acta Biomater.* **2017**, *54*, 35.
[9] M. Nikolaev, O. Mitrofanova, N. Broguiere, S. Geraldo, D. Dutta, Y. Tabata, B. Elci, N. Brandenberg, I. Kolotuev, N. Gjorevski, H. Clevers, M. P. Lutolf, *Nature* **2020**, *585*, 574.
[10] N. Gjorevski, M. Nikolaev, T. E. Brown, O. Mitrofanova, N. Brandenberg, F. W. DelRio, F. M. Yavitt, P. Liberali, K. S. Anseth, M. P. Lutolf, *Science* **2022**, *375*, eaaw9021.
[11] M. Théry, *J. Cell Sci.* **2010**, *123*, 4201.
[12] W. Xi, T. B. Saw, D. Delacour, C. T. Lim, B. Ladoux, *Nat. Rev. Mater.* **2018**, *4*, 23.
[13] E. Karzbrun, A. H. Khankhel, H. C. Megale, S. M. K. Glasauer, Y. Wyle, G. Britton, A. Warmflash, K. S. Kosik, E. D. Siggia, B. I. Shraiman, S. J. Streichan, *Nature* **2021**, *599*, 268.
[14] J. Lee, A. A. Abdeen, K. L. Wycislo, T. M. Fan, K. A. Kilian, *Nat. Mater.* **2016**, *15*, 856.
[15] S. J. P. Callens, D. Fan, I. A. J. van Hengel, M. Minneboo, P. J. Díaz-Payno, M. M. Stevens, L. E. Fratila-Apachitei, A. A. Zadpoor, *Nat. Commun.* **2023**, *14*, 855.
[16] S. J. P. Callens, R. J. C. Uyttendaele, L. E. Fratila-Apachitei, A. A. Zadpoor, *Biomaterials* **2020**, *232*, 119739.
[17] B. L. LeSavage, R. A. Suhar, N. Broguiere, M. P. Lutolf, S. C. Heilshorn, *Nat. Mater.* **2022**, *21*, 143.
[18] C. D. Paul, P. Mistriotis, K. Konstantopoulos, *Nat. Rev. Cancer* **2017**, *17*, 131.
[19] S. van Helvert, C. Storm, P. Friedl, *Nat. Cell Biol.* **2018**, *20*, 8.
[20] P. Friedl, S. Alexander, *Cell* **2011**, *147*, 992.
[21] P. Friedl, J. Locker, E. Sahai, J. E. Segall, *Nat. Cell Biol.* **2012**, *14*, 777.
[22] P. Friedl, D. Gilmour, *Nat. Rev. Mol. Cell Biol.* **2009**, *10*, 445.
[23] E. Sahai, *Nat. Rev. Cancer* **2007**, *7*, 737.
[24] S. A. Vilchez Mercedes, F. Bocci, H. Levine, J. N. Onuchic, M. K. Jolly, P. K. Wong, *Nat. Rev. Cancer* **2021**, *21*, 592.
[25] R. Mayor, S. Etienne-Manneville, *Nat. Rev. Mol. Cell Biol.* **2016**, *17*, 97.
[26] Z. Chen, S. Kheiri, E. W. K. Young, E. Kumacheva, *Langmuir* **2022**, *38*, 6233.
[27] C. Wang, Z. Tang, Y. Zhao, R. Yao, L. Li, W. Sun, *Biofabrication* **2014**, *6*, 022001.
[28] A. Fatehullah, S. H. Tan, N. Barker, *Nat. Cell Biol.* **2016**, *18*, 246.
[29] S. E. Park, A. Georgescu, D. Huh, *Science* **2019**, *364*, 960.
[30] T. Eguchi, M. Sheta, M. Fujii, S. K. Calderwood, *Semin. Cancer Biol.* **2022**, *86*, 112.
[31] A. Ganguli, A. Mostafa, C. Saavedra, Y. Kim, P. Le, V. Faramarzi, R. W. Feathers, J. Berger, K. P. Ramos-Cruz, O. Adeniba, G. J. P. Diaz, J. Drnevich, C. L. Wright, A. G. Hernandez, W. Lin, A. M. Smith, F. Kosari, G. Vasmatzis, P. Z. Anastasiadis, R. Bashir, *Sci. Adv.* **2021**, *7*, eabc1323.
[32] G. Mehta, A. Y. Hsiao, M. Ingram, G. D. Luker, S. Takayama, *J. Controlled Release* **2012**, *164*, 192.
[33] T. Rodrigues, B. Kundu, J. Silva-Correia, S. C. Kundu, J. M. Oliveira, R. L. Reis, V. M. Correlo, *Pharmacol. Ther.* **2018**, *184*, 201.
[34] E. Prince, S. Kheiri, Y. Wang, F. Xu, J. Cruickshank, V. Topolskaia, H. Tao, E. W. K. Young, A. P. McGuigan, D. W. Cescon, E. Kumacheva, *Adv. Healthcare Mater.* **2022**, *11*, 2101085.
[35] S. Kheiri, E. Kumacheva, E. W. K. Young, *Frontiers in Bioeng. and Biotechnol.* **2021**, *9*, 781566.
[36] Y. Wang, M. Liu, Y. Zhang, H. Liu, L. Han, *Lab Chip* **2023**, *23*, 1080.
[37] W. Liu, J. C. J. J.-C. Wang, J. C. J. J.-C. Wang, *Lab Chip* **2015**, *15*, 1195.
[38] W. Du, L. Li, K. P. Nichols, R. F. Ismagilov, *Lab Chip* **2009**, *9*, 2286.
[39] S. Kheiri, Z. Chen, I. Yakavets, F. Rakhshani, E. W. K. Young, E. Kumacheva, *Biotechnol. J.* **2023**, *18*, 2200621.
[40] N. Matsumoto, M. Ogawa, K. Takayasu, M. Hirayama, T. Miura, K. Shiozawa, M. Abe, H. Nakagawara, M. Moriyama, S. Udagawa, *J Med Ultrasonics* **2015**, *42*, 505.
[41] R. L. F. Amaral, M. Miranda, P. D. Marcato, K. Swiech, *Frontiers in Physiol.* **2017**, *8*, 605.
[42] H. L. Hiraki, D. L. Matera, W. Y. Wang, E. S. Prabhu, Z. Zhang, F. Midekssa, A. E. Argento, J. M. Buschhaus, B. A. Humphries, G. D. Luker, A. Pena-Francesch, B. M. Baker, *Acta Biomater.* **2022**, *163*, S1742706122006122.
[43] D. B. Agus, J. F. Alexander, W. Arap, S. Ashili, J. E. Aslan, R. H. Austin, V. Backman, K. J. Bethel, R. Bonneau, W.-C. Chen, C. Chen-Tanyolac, N. C. Choi, S. A. Curley, M. Dallas, D. Damania, P. C. W. Davies, P. Decuzzi, L. Dickinson, L. Estevez-Salmeron, V. Estrella, M. Ferrari, C. Fischbach, J. Foo, S. I. Fraley, C. Frantz, A. Fuhrmann, P. Gascard, R. A. Gatenby, Y. Geng, S. Gerecht, et al., *Sci. Rep.* **2013**, *3*, 1449.
[44] T. Lecuit, P.-F. Lenne, *Nat. Rev. Mol. Cell Biol.* **2007**, *8*, 633.
[45] B. Ladoux, R.-M. Mège, *Nat. Rev. Mol. Cell Biol.* **2017**, *18*, 743.
[46] A. Ravasio, I. Cheddadi, T. Chen, T. Pereira, H. T. Ong, C. Bertocchi, A. Brugues, A. Jacinto, A. J. Kabla, Y. Toyama, X. Trepat, N. Gov, L. Neves de Almeida, B. Ladoux, *Nat. Commun.* **2015**, *6*, 7683.
[47] B. W. Graf, S. A. Boppart, in *Live Cell Imaging: Methods and Protocols*, (Ed.: D. B. Papkovsky), Humana Press, Totowa, NJ, **2010**, pp. 211.
[48] E. Blauth, H. Kubitschke, P. Gottheil, S. Grosser, J. A. Käs, *Front. Phys.* **2021**, *9*, 666709.
[49] E. Lawson-Keister, M. L. Manning, *Curr. Opin. Cell Biol.* **2021**, *72*, 146.
[50] X. Wang, A. Enomoto, N. Asai, T. Kato, M. Takahashi, *Pathology International* **2016**, *66*, 183.
[51] P. Friedl, K. Wolf, J. Lammerding, *Curr. Opin. Cell Biol.* **2011**, *23*, 55.
[52] I. Saénz-de-Santa-María, L. Celada, M.-D. Chiara, *Cells* **2020**, *9*, 731.
[53] C.-F. Li, J.-Y. Chen, Y.-H. Ho, W.-H. Hsu, L.-C. Wu, H.-Y. Lan, D. S.-S. Hsu, S.-K. Tai, Y.-C. Chang, M.-H. Yang, *Nat. Cell Biol.* **2019**, *21*, 251.
[54] Q. Quan, X. Wang, C. Lu, W. Ma, Y. Wang, G. Xia, C. Wang, G. Yang, *Cancer Sci.* **2020**, *111*, 467.
[55] C. De Pascalis, S. Etienne-Manneville, *MBoC* **2017**, *28*, 1833.
[56] B. K. Byrd, V. Krishnaswamy, J. Gui, T. Rooney, R. Zuurbier, K. Rosenkranz, K. Paulsen, R. J. Barth, *Breast Cancer Res. Treat.* **2020**, *183*, 403.
[57] B. F. Kurland, E. R. Gerstner, J. M. Mountz, L. H. Schwartz, C. W. Ryan, M. M. Graham, J. M. Buatti, F. M. Fennessy, E. A. Eikman, V. Kumar, K. M. Forster, R. L. Wahl, F. S. Lieberman, *Magnetic Resonance Imaging* **2012**, *30*, 1301.
[58] R. J. Gillies, P. E. Kinahan, H. Hricak, *Radiology* **2016**, *278*, 563.
[59] J. Li, K. Zhang, Z. Shi, X. Zhang, J. Xie, J. Liu, C. Chang, *Sci. Rep.* **2018**, *8*, 9040.
[60] E. Huynh, T. P. Coroller, V. Narayan, V. Agrawal, J. Romano, I. Franco, C. Parmar, Y. Hou, R. H. Mak, H. J. W. L. Aerts, *PLoS One* **2017**, *12*, 0169172.

[61] R. El Ayachy, N. Giraud, P. Giraud, C. Durdux, P. Giraud, A. Burgun, J. E. Bibault, *The Role of Radiomics in Lung Cancer: From Screening to Treatment and Follow-Up. Front. Oncol.* **2021**, *11*, 603595.
[62] S. Wang, A. Chen, L. Yang, L. Cai, Y. Xie, J. Fujimoto, A. Gazdar, G. Xiao, *Sci. Rep.* **2018**, *8*, 10393.
[63] I. Chatzistamou, J. Rodriguez, T. Jouffroy, A. Girod, D. Point, A. Sklavounou, C. Kittas, X. Sastre-Garau, J. Klijanienko, *J. Oral Pathol. & Med.* **2010**, *39*, 667.
[64] L. Ricotti, B. Trimmer, A. W. Feinberg, R. Raman, K. K. Parker, R. Bashir, M. Sitti, S. Martel, P. Dario, A. Menciassi, *Sci. Rob.* **2017**, *2*, eaaq0495.
[65] S. P. Pașca, *Nature* **2018**, *553*, 437.
[66] S. Kanton, S. P. Pașca, *Development* **2022**, *149*, dev201120.
[67] M. R. Blatchley, K. S. Anseth, *Nat Rev Bioeng* **2023**, *1*, 329.
[68] N. A. Mayr, W. T. C. Yuh, T. Taoka, J. Z. Wang, D. H. Wu, J. F. Montebello, S. L. Meeks, A. C. Paulino, V. A. Magnotta, M. Adli, J. I. Sorosky, M. V. Knopp, J. M. Buatti, *Am. J. Roentgenol.* **2006**, *187*, 65.
[69] E. Prince, J. Cruickshank, W. Ba-Alawi, K. Hodgson, J. Haight, C. Tobin, A. Wakeman, A. Avoulov, V. Topolskaia, M. J. Elliott, A. P. McGuigan, H. K. Berman, B. Haibe-Kains, D. W. Cescon, E. Kumacheva, *Nat. Commun.* **2022**, *13*, 1466.
[70] A. Perperoglou, W. Sauerbrei, M. Abrahamowicz, M. Schmid, *BMC Med. Res. Methodol.* **2019**, *19*, 46.